






Stable, active CO₂ reduction to formate via redox-modulated stabilization of active sites

Le Li^{1,5}, Adnan Ozden^{2,5}, Shuyi Guo³, F. Pelayo García de Arquer ⁴, Chuanhao Wang¹, Mingzhe Zhang¹, Jin Zhang¹, Haoyang Jiang¹, Wei Wang ³, Hao Dong ³✉, David Sinton ², Edward H. Sargent ⁴✉ & Miao Zhong¹✉

Electrochemical reduction of CO₂ (CO₂R) to formic acid upgrades waste CO₂; however, up to now, chemical and structural changes to the electrocatalyst have often led to the deterioration of performance over time. Here, we find that alloying p-block elements with differing electronegativities modulates the redox potential of active sites and stabilizes them throughout extended CO₂R operation. Active Sn-Bi/SnO₂ surfaces formed in situ on homogeneously alloyed Bi_{0.1}Sn crystals stabilize the CO₂R-to-formate pathway over 2400 h (100 days) of continuous operation at a current density of 100 mA cm⁻². This performance is accompanied by a Faradaic efficiency of 95% and an overpotential of ~ -0.65 V. Operating experimental studies as well as computational investigations show that the stabilized active sites offer near-optimal binding energy to the key formate intermediate *OCHO. Using a cation-exchange membrane electrode assembly device, we demonstrate the stable production of concentrated HCOO⁻ solution (3.4 molar, 15 wt%) over 100 h.

¹College of Engineering and Applied Sciences, National Laboratory of Solid State Microstructures, Collaborative Innovation Center of Advanced Microstructure, Jiangsu Key Laboratory of Artificial Functional Materials, Nanjing University, Nanjing, China. ²Department of Mechanical and Industrial Engineering, University of Toronto, Toronto, Ontario, Canada. ³Kuang Yaming Honors School & Institute for Brain Sciences, Nanjing University, Nanjing, China. ⁴Department of Electrical and Computer Engineering, University of Toronto, Toronto, Ontario, Canada. ⁵These authors contributed equally: Le Li, Adnan Ozden. ✉email: donghao@nju.edu.cn; ted.sargent@utoronto.ca; miaozhong@nju.edu.cn

Electrochemical CO₂ reduction (CO₂R) driven by electrical energy converts CO₂ into low carbon footprint chemicals and fuels¹. Among CO₂R products, formic acid (HCOOH) or formate (HCOO⁻) is used in pharmaceutical, electrolytic metallurgy, leather, and fuel cell applications^{2–6}. HCOO⁻ has a high market value per energy (cents/kWh)⁷, making it a candidate of particular interest.

Conventionally, HCOO⁻ is produced from the hydrolysis of methyl formate, which uses CH₃OH and CO as starting materials. This chemical reforming process requires strict reaction conditions and high energy input^{8–10}. In contrast, CO₂R requires only CO₂, water, and electrical energy^{7,11,12}. Unfortunately, to date, CO₂R catalysts and systems favouring HCOO⁻ have not achieved the required combination of high selectivity (Faradaic efficiency (FE))¹³, high reaction rate (current density)¹³, high energy efficiency (EE)¹⁴, and, in particular, long-term stability.

Among electrocatalytic materials studied, Sn is a promising candidate owing to its low cost and planetary abundance^{15,16}. Sn has strong binding energy for *OCHO, and this favours the first-step CO₂ hydrogenation in CO₂-to-formate conversion^{17,18}. The second step electron transfer requires high energy to reduce *OCHO to HCOO⁻, resulting in a large overpotential and consequently a low EE. Sn has medium binding energy to *COOH and *H, which makes it difficult to fully suppress CO and H₂ generation; the FE for HCOO⁻ has therefore been limited to 80–85%. Recent studies of Sn-based core-shell structures, including Ag-Sn¹⁹, Cu-Sn²⁰, Bi-Sn²¹, and phase-segregated bimetallic systems^{22,23}, showed improved FE for HCOO⁻. Further improvement of the HCOO⁻ production rate and cathodic energy efficiency (CEE) relative to current benchmarks (Supplementary Table 4) requires precise control of the elemental distributions in the active sites. In particular, knowledge of the electrochemical stability of Sn and Sn-based materials in aqueous electrolytes at different pH is lacking; indeed, among reported formate catalysts, it has been challenging to combine optimal

adsorption energetics for intermediate binding with sites stable against reconstruction^{13–16}.

Here, we present active Sn-Bi/SnO₂ surfaces that are grown conformally on uniformly alloyed Bi_{0.1}Sn crystals. These surfaces support the stable reduction of CO₂ to formate over a period in excess of 2400 h (100 days) of continuous operation, with a near-unity formate FE of over 95% and a CEE exceeding 70% at a current density of 100 mA cm⁻² in 1 M potassium bicarbonate (KHCO₃) and potassium hydroxide (KOH) electrolytes at pH 11. This stability and CEE is significantly improved compared to literature benchmarks^{13,24–27}. The selectivity and energy efficiency obtained to meet the performance required for a positive net present value in an economic analysis of formate production¹¹. Computational studies reveal that, across a wide range (1.5–12.5%) of Bi incorporation into Sn, the facets of Sn-Bi alloys and Sn-Bi/SnO₂ composites provide sites with near-optimal binding energy to *OCHO. This approach lowers the reaction energy in CO₂-to-formate conversion. The by-products CO and H₂ are suppressed due to their increased reaction energy on Sn-Bi alloys. The redox-modulated Sn-Bi/SnO₂ surfaces remain active and protect Bi_{0.1}Sn catalysts against corrosion or reconstruction during extended CO₂R. We further demonstrate stable production of 3.4 molar (15 wt%) HCOO⁻ (formate) solution of over 100 h at a constant current density of 60 mA cm⁻² with an average full-cell EE of ~27% in a membrane electrode assembly (MEA) system based on a cation-exchange membrane (CEM), highlighting that Bi_{0.1}Sn catalysts are reliable for long-lasting HCOO⁻ (formate) production in different CO₂R systems.

Results

Characterization. We used thermal evaporation to produce Bi_xSn ($x = 0.1, 0.2, 0.3$), Bi, and Sn precatalysts on polytetrafluoroethylene (PTFE) gas diffusion substrates (Supplementary Fig. 1). Dense and compact particle-film layers were formed for all Bi_xSn ($x = 0.1, 0.2, 0.3$), Bi, and Sn catalysts, ensuring electrical conductivity for CO₂R (Supplementary Fig. 2). The particle size is 200–300 nm for the Bi and 1–1.5 μm for the Sn catalyst. Bi_{0.2}Sn and Bi_{0.3}Sn possess similar particle sizes of 1–1.5 μm to that of Sn, but they fail to form a uniform alloy; Bi precipitates over a large area (Supplementary Figs. 3, 4). Bi_{0.1}Sn forms uniform crystals with particle sizes of 700–1000 nm, as confirmed by scanning electron microscopy (SEM), transmission electron microscopy (TEM) images, and scanning transmission electron microscopy energy dispersive spectroscopy (STEM-EDS) elemental mapping in Fig. 1b, c, e. The selected area electron diffraction (SAED) pattern of Bi_{0.1}Sn exhibits distinct single-crystal diffraction spots corresponding to the Sn plane indexes (Fig. 1d), suggesting that Bi is incorporated into the Sn crystals. The facets exposed are primarily (200) and (101), consistent with the observations from high-resolution TEM analysis (Fig. 1c). We carried out STEM-EDS, SEM-EDS, and XPS analyses, and obtained similar Bi concentrations of ~10 at.% for the Bi_{0.1}Sn catalyst (Supplementary Figs. 5–9 and Table 1), suggesting that Bi and Sn are uniformly distributed from the surface to the bulk.

Density functional theory (DFT) calculations. In light of the above characterizations, we built models and performed DFT studies to calculate the reaction energy on Bi, Sn, and Bi_ySn₆₄

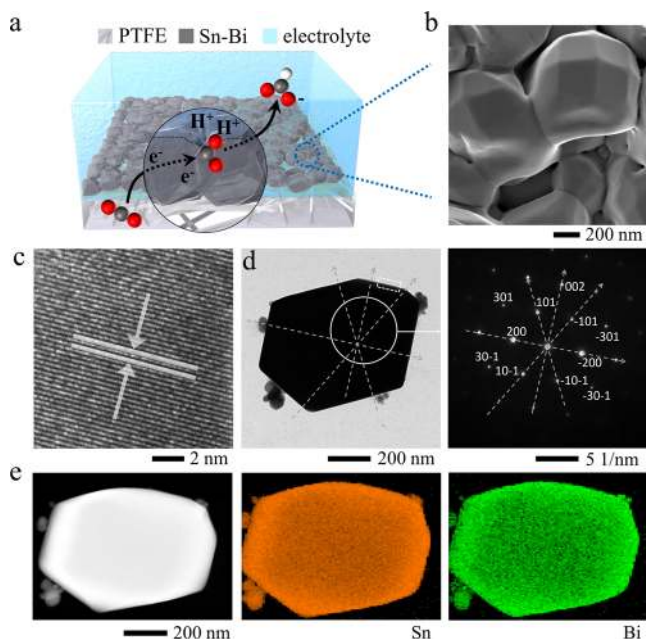


Fig. 1 Structural and elemental analyses of Bi_{0.1}Sn electrocatalysts. **a** Schematic of Bi_{0.1}Sn electrocatalyst on a polytetrafluoroethylene gas diffusion layer for electroreduction of CO₂. **b** SEM, **c** HRTEM, **d** TEM, SAED, and, **e** STEM, EDS analyses of Bi_{0.1}Sn electrocatalyst. The high-resolution TEM image in (c) shows the lattice fringes corresponding to the Sn (200) facet. The dashed box in (d) is the location to take the HRTEM.

Table 1 The molar concentration of Bi and Sn in the Bi_{0.1}Sn obtained by XPS, SEM-EDS, and TEM-EDS analyses.

	TEM-EDX	SEM-EDX	XPS
Bi: Sn (at.%)	~0.15:1	~0.1:1	~0.12:1

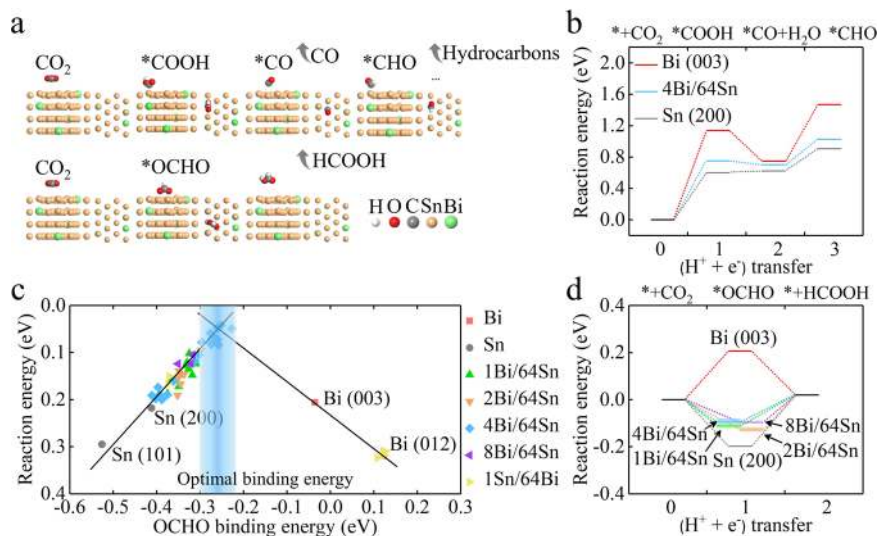


Fig. 2 DFT calculations. **a** Possible pathways of electrochemical CO₂ reduction. The top panel shows the *COOH pathway to produce CO, CH₄, or C₂₊ hydrocarbons. The bottom panel shows the *OCHO pathway to produce HCOO⁻. Bi, Sn, C, O, and H atoms are represented by green, yellow, grey, red, and white spheres, respectively. **b** Reaction energy for CO formation on Bi (003), Sn (200), and Bi₄Sn₆₄ (200) surfaces without applying any external potential ($U = 0$ eV). **c** The volcano plot describing *OCHO adsorption energy versus CO₂-to-HCOO⁻ reaction energy. **d** Reaction energy for HCOO⁻ formation on Bi (003), Sn (200), and Bi_{*y*}Sn₆₄ ($y = 1, 2, 4, 8$) surfaces without applying any external potential ($U = 0$ eV).

($y = 1, 2, 4, 8$) surfaces (details in Supplementary Figs. 10–15 and Supplementary Table 1). As shown in Fig. 2a, the production of CO, CH₄, and other C₂₊ hydrocarbons generally proceeds via the *COOH intermediate pathway^{28,29}. *COOH adsorption requires the outer shell electrons of catalysts to have both energy that matches the LUMO energy of CO₂, and electronic orbitals that overlap with molecular orbitals of the C–O π bond. Production of HCOO⁻ often occurs via the *OCHO intermediate pathway^{14,18}. This requires catalysts to possess suitable binding energy to O. Bi and Sn are both p-block metals that, as shown in Fig. 2b, d, display significantly uphill reaction energy to *COOH compared to that to *OCHO, indicating that HCOO⁻ is the major product.

Since the intermediate *OCHO is energetically more favourable than *COOH on Bi, Sn, and Bi_{0.1}Sn surfaces, we examined their reaction energy for HCOO⁻ production in detail. Figure 2d reveals that Bi (003) tends to bind *OCHO too weakly, that Sn (002) may bind *OCHO too strongly, and that of the calculated BiSn slabs, Bi₄Sn₆₄ and Bi₈Sn₆₄ show the optimal binding energy to *OCHO of near to -0.13 eV, indicating low reaction energy for the CO₂-to-HCOO⁻ conversion. We plotted the reaction energy of different catalyst archetypes as a function of their adsorption energy to *OCHO at 298 K and 1 atm. (Fig. 2c). We took an average of the binding energy on enumerated possible configurations and present the averaged binding energy in Fig. 2d. Bi_{*y*}Sn₆₄ ($y = 1, 2, 4, 8$), with a relatively wide range of Bi ratios in different Sn facets, exhibits an abundance of adsorption sites with improved *OCHO binding energy that enhances CO₂ reduction (DFT calculation details are given in Supplementary Figs. 12–15). The volcano relationship predicts that Bi₄Sn₆₄ (incorporation of 6.25% Bi into Sn) may be the most active (Supplementary Table 2). We further find that Bi₄Sn₆₄ elevates the reaction energy to CO and H₂, suppressing the generation of CO, H₂, and C₂₊ hydrocarbons (Fig. 2b and Supplementary Fig. 11). In summary, our computational simulations point to the alloying of Sn with Bi as a strategy to enhance HCOO⁻ production.

CO₂R in aqueous flow cells. The CO₂R performance of Bi_{*x*}Sn alloys ($x = 0.1, 0.2, 0.3$), as well as pure Bi or Sn control samples, was first evaluated in 1 M KOH electrolyte (pH = 14) in a flow-cell electrolyser. Ag/AgCl electrodes were used as the reference

electrodes, and commercial Ni foams were used as the anodes for the water oxidation reaction in a three-electrode setup. Linear sweep voltammetry (LSV) curves obtained from 0 V to -2 V vs. reversible hydrogen electrode (V_{RHE}) show that Bi_{0.1}Sn has the most positive onset potential for CO₂R (Fig. 3a and Supplementary Fig. 16a). This is consistent with the DFT calculations that incorporating 1.5–12.5% Bi into Sn lowers the reaction energy in the electrochemical CO₂-to-formate conversion (Fig. 2). A rapid increase of the cathodic current is observed with Bi_{0.1}Sn at potentials more negative than $-0.5 V_{\text{RHE}}$. To study the electrochemical characteristics of the Bi_{0.1}Sn, Bi, and Sn catalysts, we carried out the electrochemical active surface area (ECSA), and electrochemical impedance spectroscopy (EIS) analyses³⁰. The estimated ECSAs of Bi and Bi_{0.1}Sn are twice as large as that of Sn (Supplementary Fig. 17). Also, Bi_{0.1}Sn has the lowest interface resistance (Supplementary Fig. 18). These results confirm that Bi_{0.1}Sn reduces the potential loss and, consequently, improves the CEE.

To quantify the FEs of CO₂R products, Bi_{*x*}Sn ($x = 0.1, 0.2, 0.3$), Bi, and Sn catalysts were evaluated in a chronopotentiometry mode by applying current densities of 100, 200, and 300 mA cm⁻². Gaseous and liquid products were quantified by gas chromatography (GC) and nuclear magnetic resonance (NMR), respectively. As shown in Fig. 3b and Supplementary Fig. 16b, the Bi_{0.1}Sn catalyst shows over 95% FE for HCOO⁻ in a wide range of current densities. Only a small amount of H₂ and CO was detected, and no other liquid products were formed (Supplementary Figs. 19, 20). A CO₂-to-formate CEE of $\sim 75\%$ was achieved at pH 14 at 100 mA cm⁻². Under similar conditions, Bi_{0.2}Sn, Bi_{0.3}Sn, and Bi catalysts produce 95% FE for HCOO⁻, but they require a more negative potential for the same current density (Supplementary Fig. 16b, 21 and Supplementary Table 3). The Sn catalyst produces an FE of $\sim 85\%$ for HCOO⁻, along with a constant total FE of $\sim 15\%$ for H₂ and CO. It also requires a more negative potential to reach 100 mA cm⁻², and thus the CEE for HCOO⁻ is limited to 50%.

To assess the stability of the Bi_{0.1}Sn catalyst during CO₂R, carbon nanoparticles (NPs) and graphite were coated on the Bi_{0.1}Sn/PTFE electrode to form a hybrid structure of graphite/carbon NPs/Bi_{0.1}Sn/PTFE. This structure enables uniform distribution of the electrolyte and electrical current over the

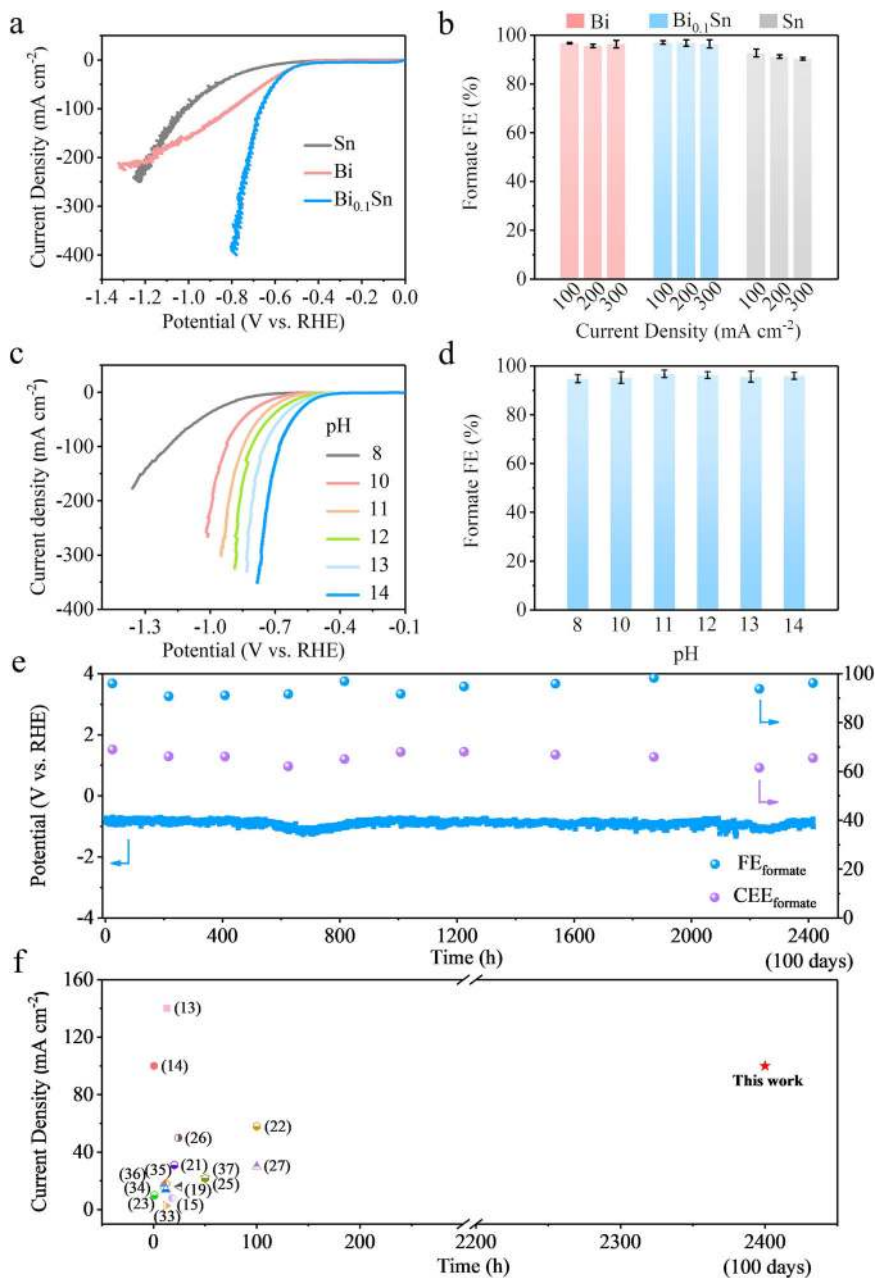


Fig. 3 CO₂ electroreduction performance using Bi_{0.1}Sn, Bi, and Sn catalysts. **a** Linear sweep voltammetry curves of Bi_{0.1}Sn, Bi, and Sn in 1 M KOH electrolyte. **b** The corresponding formate FEs under different current densities. **c** Linear sweep voltammetry curves. **d** The corresponding formate FEs in 1 M KHCO₃ and KOH electrolytes at different pH (pH = 8, 10, 11, 12, 13, and 14) at a current density of 100 mA cm⁻². **e** The CO₂-reduction chronopotentiometry curve (blue line), CO₂-to-formate FE (blue dots), and CO₂-to-formate half-cell energy conversion efficiency (purple dots) in 1 M KHCO₃ and KOH electrolyte at pH = 11 at an applied current density of 100 mA cm⁻². **f** Comparison of our work with previously published data. Error bars correspond to the standard deviation of five independent measurements.

Bi_{0.1}Sn surfaces^{31,32}. Note that the coated carbon nanoparticles and graphite are not CO₂R electrocatalysts and they don't produce any formate under our CO₂R operating conditions. Importantly, we coated carbon nanoparticles and graphite for all the Bi, Sn, and Bi_{0.1}Sn catalysts, comparing their CO₂R activity under the same working conditions. We are therefore certain that the performance obtained solely represents the properties of each catalyst. We also kept the electrolyte pH unchanged during the long-term CO₂R stability test so that the CO₂R results are all compared under the same pH conditions. In our studies, Bi_{0.1}Sn catalyst produces HCOO⁻ with an FE exceeding 95% for over 170 h at 100 mA cm⁻² and an overpotential of ~-0.5 V_{RHE} in 1 M

KOH electrolyte (Supplementary Fig. 22). Control experiments for Bi and Sn samples using similar carbon/graphite coatings led to both lower CEEs and worse stability within 50–70 h (see Supplementary Methods and Supplementary Figs. 23–25).

To evaluate the effect of pH on the activity and stability of CO₂R, we studied the performance of Bi_{0.1}Sn catalysts in KHCO₃ and KOH electrolytes at different pH levels (see the Supplementary Methods for details). As shown in Supplementary Fig. 26, the formate FEs are above 90% at all pH (8–14) at current densities from 25 to 300 mA cm⁻². This indicates that the formate FE is directly related to the properties of catalysts because the CO₂R kinetics are more favourable than those of the competing

hydrogen evolution reaction under these working conditions. The use of alkaline electrolytes also shifts the working potential positively with the increase of electrolyte pH. As shown in Figs. 3c, 3d and Supplementary Fig. 27, the CEEs for HCOO⁻ are above 70% at 100 mA cm⁻² at pH greater than 11. We performed 100-hour stability tests at varying pH (11–14) at a current density of 100 mA cm⁻² and analysed their surface morphology, composition, and other material properties after the reaction by SEM, XRD, XPS, and EDX (Supplementary Figs. 28–31). At pH 11, the morphology change is minor compared to those at higher pH levels after 100 h of operation. This is in line with the Pourbaix diagram (Supplementary Fig. 32), in which both metallic Bi and Sn are cathodically protected at potentials more negative than $-0.35 V_{\text{RHE}}$ at pH 11. The self-corrosion potentials of Bi_{0.1}Sn catalysts at pH 11–14 in Supplementary Fig. 34 indicate that, thermodynamically, the tendency of corrosion increases with the increase of pH.

Remarkably, we achieved efficient CO₂R over 2400 h (100 days) at pH 11 with stable 70% CEE (Fig. 3e). A full-cell EE of 35% (without IR correction) was obtained using unmodified, commercial Ni foams as anodes for the water oxidation reaction in a flow-cell system (Supplementary Fig. 35). This is significant in developing CO₂R electrolyzers that meet the long operational stability requirements for commercialization¹² of at least 1000 h with current densities exceeding 100 mA cm⁻². Ours is the first demonstration of CO₂R stability achieving this goal. To put our results in a broader context, we plotted our data with reported values^{13–15,19,21–23,25–27,33–37} in Fig. 3f. The stability and CEE at current densities $\geq 100 \text{ mA cm}^{-2}$ we achieved outperform literature benchmarks by two orders of magnitude, indicating a critical milestone in the field of CO₂R field.

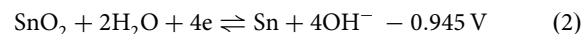
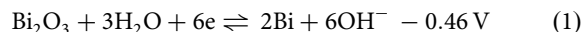
We compared the CO₂R performance of Bi and Sn at 100 mA cm⁻² and in 1 M KHCO₃ and KOH electrolytes at pH 11. Sn produces $\sim 80\%$ FE for HCOO⁻ with a constant total FE of $\sim 20\%$ for H₂ and CO. The hydrogen evolution reaction increases and HCOO⁻ decreases throughout electrolysis (Supplementary Fig. 37). Bi produces 95% FE for HCOO⁻, but the CEE is much lower (Supplementary Figs. 36, 37). We found that the stability of Bi was poor: We performed 10 independent tests for Bi samples in an aqueous system with a continuous operation of 100 h. We observed performance decay and peeling off of Bi in all tests (Supplementary Fig. 38).

To diagnose the origins of catalyst instability during CO₂R, we compared Bi and Bi_{0.1}Sn catalysts before and after the reactions. After the 70-h test, the original 200–500 nm Bi crystals were completely reconstructed to 20–50 nm nanoparticles with a large amount of O on the surfaces (Fig. 4a–c). SEM-EDX and HRTEM analyses reveal that polycrystalline Bi₂O₃ was formed on Bi, which is in line with the XRD results for Bi after the reaction; the yellow line in the HRTEM image indicates the boundary between the Bi bulk and the Bi₂O₃ surface (Fig. 4b, c and Supplementary Figs. 39–40). This chemical and structural transformation is associated with effects involving (i) the non-uniform distribution of electrical potential on the surfaces during the reaction^{38,39} and (ii) the existence of OH⁻ near Bi at pH 11 to make redox reactions between Bi and Bi₂O₃ continuously occur. Metastable Bi failed to form equilibrated phases on the surfaces and, thus, Bi was continuously reconstructed during the reaction. The reconstructed Bi₂O₃/Bi nanoparticles show increased electrical resistance to decrease the overall performance. As shown in the XPS depth profile studies, Bi³⁺ was detected on the 50h-reaction Bi throughout three rounds of the 3–5 nm soft Ar etching (Fig. 4h). This gives evidence that Bi³⁺ is presented in the bulk of the 50h-reaction Bi sample. In contrast, when we studied the evaporated Bi catalyst before reaction, Bi³⁺ disappeared after one round of $\sim 3\text{--}5 \text{ nm}$ soft Ar etching, indicating that the top surface Bi was

oxidized in air and no bulk oxidation was observed (Supplementary Fig. 41). DFT studies in Supplementary Fig. 42 reveal that the Bi₂O₃ (002) and (210) facets largely shift the *OCHO reaction energy to ~ -0.83 and ~ 0.30 eV, which is either too strong or too weak for the reaction as predicted by the volcano relationship in Fig. 2c. Taking these together with SEM, TEM, and electrochemical analyses for the Bi control samples before and after the reaction in Fig. 4b, c and Supplementary Figs. 38, 39, we conclude that Bi reconstructed to Bi₂O₃/Bi during the reduction, which leads to performance degradation and eventually catalyst peeling off.

In contrast, the Bi_{0.1}Sn catalyst remains stable during the long CO₂R operation under the same working conditions. After our tests, Bi_{0.1}Sn remains intact on PTFE with morphology preserved (Fig. 4d–f and Supplementary Fig. 43). Dark-field and bright-field TEM images with SAED patterns and HRTEM visualized conformal $\sim 20\text{--}50 \text{ nm}$ SnO₂/Sn-Bi mixture layers on Bi_{0.1}Sn surfaces (Fig. 4g and Supplementary Figs. 44–46). The SAED patterns show a polycrystalline nature of surface SnO₂, in line with the XRD results (Supplementary Figs. 47, 44c). We carried out calculations of different initial configurations with O involved in the Sn-Bi system on the surface (Supplementary Fig. 48). The results reveal that the homogeneously alloyed Bi_{0.1}Sn crystal with few O atoms involved on the surfaces shows similar catalytic performance to that of the metallic Bi_{0.1}Sn crystal. DFT studies also reveal that the SnO₂ (110) facet remains active for HCOO⁻ production with the optimal binding energy of ~ -0.15 eV for *OCHO (Supplementary Fig. 42).

As shown in the XPS depth profiles (Fig. 4i and Supplementary Fig. 49), after a round of $\sim 3\text{--}5 \text{ nm}$ soft Ar etching, Bi⁰, Sn⁰ and Sn⁴⁺ were observed in the consequent three rounds of the 3–5 nm soft Ar etching. The electrochemical redox potentials of Bi/Bi³⁺ and Sn/Sn⁴⁺ are

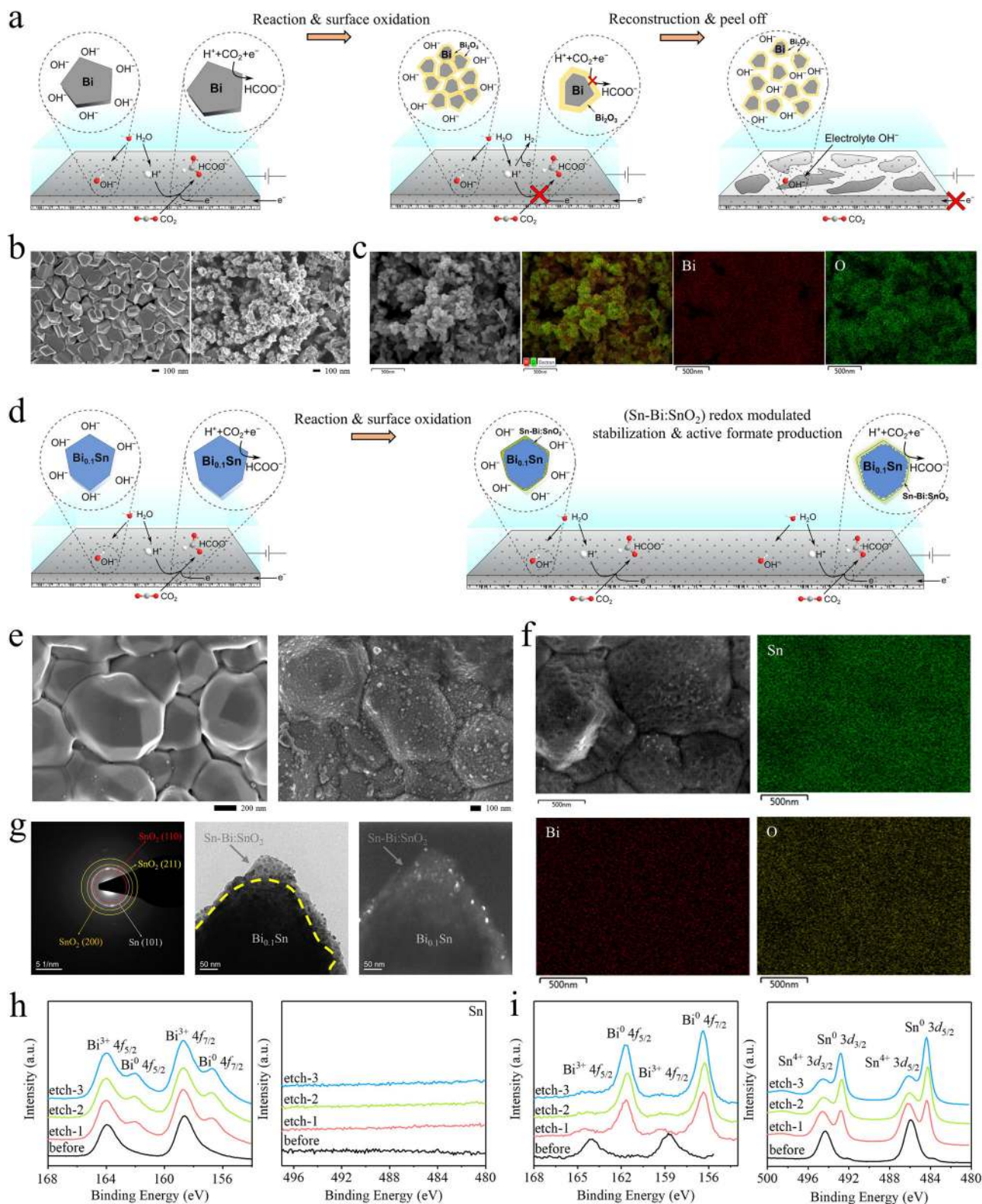


This suggests that Sn should be oxidized before Bi. A redox-modulated balance between Sn and SnO₂ was formed on the bimetallic active sites on the surface during CO₂R. The redox modulation between Sn/Sn⁴⁺ protects the active BiSn:SnO₂ against corrosion. We, therefore, suggest that we in situ formed immobilized, conformal and active BiSn:SnO₂ surfaces during CO₂ reduction, being stable against chemical and structural change throughout extended CO₂R reaction over 2400 h of continuous operation.

After 2400 h, we observed densely packed Bi_{0.1}Sn particles over the electrode with clear surface Bi and Sn signals identified by XPS (Supplementary Fig. 50). No significant leaching of Bi and Sn into solution was detected via inductively coupled plasma atomic emission spectroscopy (ICP-AES) analysis (Supplementary Fig. 51). We also provide SEM images and performance curves of Bi_{0.1}Sn and Bi after different times taken from the stability tests as shown in Supplementary Fig. 52. We witness no peeling of the catalyst during the 2400 h test.

Note that a stable and efficient CO₂R device requires stable and efficient reactions of CO₂R and water oxidation. On the cathode side, Bi_{0.1}Sn catalysts deliver excellent CO₂R stability and activity via redox-modulated stabilization of active sites. On the anode side, it is vital to improving the stability and efficiency of the catalysts.

CO₂R in MEA systems. To produce concentrated HCOO⁻ solutions, we assessed the CO₂R performance of Bi, Sn, and Bi_{0.1}Sn catalysts in an MEA system (Fig. 5a, b). We first used an anion-exchange membrane (AEM) to test the MEA performance.



As shown in Fig. 5c, d, and Supplementary Table 5, Bi_{0.1}Sn produced over 90% FE for HCOO⁻ in a wide range of current densities from 30 to 180 mA cm⁻². A peak FE for HCOO⁻ of 97.8% was achieved at a current density of 120 mA cm⁻² with a full-cell potential (without IR correction) of -3.6 V and a full-cell EE of 36%. As control experiments, pristine Bi and Sn delivered peak HCOO⁻ FEs of 95.8% and 93.5% at the same current density of 120 mA cm⁻², but they required more negative potentials of

-4.1 V and -4.3 V. As a result, the full-cell EEs for the MEAs using Bi and Sn catalysts were both lower, 31% and 29%, respectively. LSV curves confirmed the CO₂R performance of Bi_{0.1}Sn surpassed those of Bi and Sn in AEM-based MEA (Supplementary Fig. 53).

We then sought to translate the champion performance of Bi_{0.1}Sn to a CEM-based MEA electrolyser as a strategy to minimize the crossover of HCOO⁻ (formate) to the anode side to

Fig. 4 Structural and elemental analyses of the Bi and Bi_{0.1}Sn electrocatalyst before and after CO₂ reduction at pH 11 and a current density of 100 mA cm⁻². **a** Schematic of Bi reconstruction during the electrochemical reaction. **b** SEM results of the as-prepared Bi nanoplates, and the reconstructed Bi/Bi₂O₃ core/shell nanoparticles after 70 h of reaction. **c** SEM-EDX elemental mapping results of the Bi/Bi₂O₃ catalysts after 70 h of reaction. **d** Schematic of a redox-modulated Bi_{0.1}Sn/SnO₂ surface on Bi_{0.1}Sn during the electrochemical reaction. **e** SEM results of the as-prepared Bi_{0.1}Sn crystals, and the (Bi_{0.1}Sn/SnO₂)/Bi_{0.1}Sn particles over 100 h of reaction. **f** SEM-EDX elemental mapping results of the (Sn-Bi/SnO₂)/Bi_{0.1}Sn catalyst over 100 h of reaction. **g** The SAED pattern, bright-field and dark-field TEM images of the Sn-Bi/SnO₂ catalysts over 100 h of reaction. **h** XPS depth profiles of the post-reaction Bi after 50-h CO₂ reduction at 100 mA cm⁻² in 1 M KHCO₃ and KOH electrolytes at pH = 11. **i** XPS depth profile of the post-reaction Bi_{0.1}Sn after 100-h CO₂ reduction at 100 mA cm⁻² in 1 M KHCO₃ and KOH electrolytes at pH = 11. The black, red, green and blue lines represent the XPS data before etching (black) and after different time courses of soft Ar etching (red, green, blue), respectively. The etched depth in each soft Ar etching is ~3–5 nm.

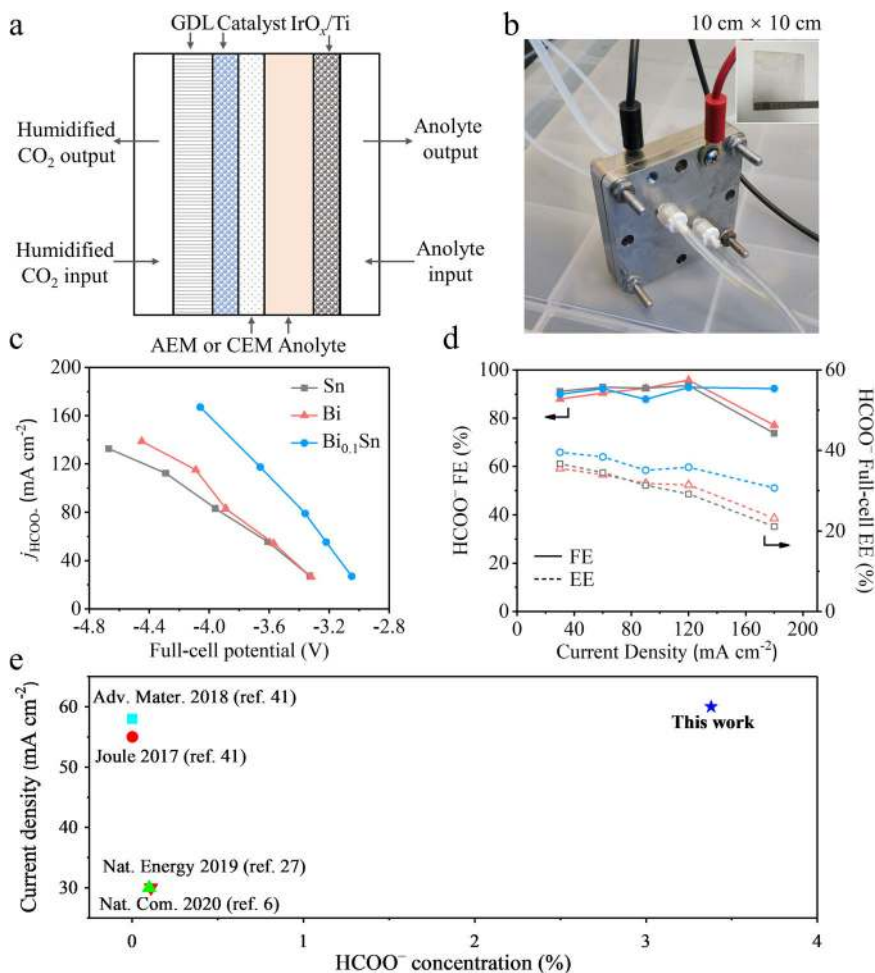


Fig. 5 CO₂ electroreduction performance in anion-exchange membrane (AEM)-based MEA systems. **a** Schematic of the MEA configuration. **b** The optical image of an MEA device. **c** Current densities vs. applied potentials of Bi, Sn, and Bi_{0.1}Sn in AEM-based MEA systems. **d** HCOO⁻ FEs and EEs of Bi, Sn, and Bi_{0.1}Sn at different current densities in AEM-based MEA systems. **e** Comparison of our data with literature benchmarks (We plot the concentration values obtained in the longest duration tests in each report).

producing a concentrated HCOO⁻ solution at the cathodic stream (HCOO⁻: 3.4 molar, 15 wt%). Replacing AEM with CEM likely changed the local pH near the catalyst surfaces during the reaction, leading to a shift of peak HCOO⁻ FE to relatively lower current densities^{7,40}. By using a high anolyte flow rate of 15 mL/min., we obtained a peak HCOO⁻ FE of ~90% at 60 mA cm⁻² with Bi_{0.1}Sn (Supplementary Fig. 54 and Supplementary Table 5). We then optimized the single-pass flow rate of anolyte (0.1 M KHCO₃) to 1.5 mL/min. to promote the HCOO⁻ concentration at the cathodic liquid stream. This optimization established a balance between membrane hydration and K⁺ availability near the catalyst surface, enabling the collection of concentrated HCOO⁻ directly from the cathodic stream. We obtained an average HCOO⁻ FE of 82% (or 4.49 mmol/h) at 60 mA cm⁻²

during 100 h of CO₂R with an average HCOO⁻ concentration of 3.4 molar (15 wt%) (Supplementary Fig. 55). This represents a 30-fold improvement in HCOO⁻ concentration with 100-hour stability along with a 2-fold increase in current density compared to the literature benchmarks reported in duration tests^{6,27,41,42} (Fig. 5e).

Discussion

We present redox-modulated, stable, and active Sn-Bi/SnO₂ surfaces on uniformly alloyed Bi_{0.1}Sn crystals, and these catalysts show a combination of high activity and performance stability in the CO₂-to-HCOO⁻ reduction exceeding 2400 h (100 days) of continuous operation. We use DFT calculations to explain that the stabilized active sites improve *OCHO binding energy and fine-

tune *COOH and *H binding energy for selective HCOO⁻ production. We show stable production of concentrated HCOO⁻ (formate) of 3.4 molar with Bi_{0.1}Sn catalysts in a solid-state CEM-based MEA system over 100 h. Our demonstration of a stable catalyst and system is a crucial step to deliver reliable and long-lasting CO₂R technology. Further efforts will be necessary to increase CO₂ single-pass yield and to the broader applicability of this system in the production of other C₂₊ liquid fuels and beyond.

Methods

Synthesis. Bi_xSn ($x = 0.1, 0.2, 0.3$), Bi, and Sn electrocatalysts were synthesized using thermal evaporation (SKY-RH400). In brief, to fabricate the Bi_xSn ($x = 0.1, 0.2, 0.3$) catalysts, different amounts of Sn and Bi were co-evaporated onto the PTFE substrates under the pressure of 10⁻⁵ Torr. The Bi evaporation rate was set to 0.1 nm s⁻¹, and the Sn evaporation rate was set to 1 nm s⁻¹, 0.5 nm s⁻¹ and 0.3 nm s⁻¹ to make the Bi_xSn ($x = 0.1, 0.2, \text{ and } 0.3$) samples. The thickness of the deposited Bi_xSn layers was ~700 nm. The pure Bi and Sn films with the same film thicknesses were prepared at an evaporation rate of ~0.3 nm s⁻¹ under the pressure of 10⁻⁵ Torr.

Characterization. SEM images were taken using a Gemini500 SEM at an accelerating voltage of 2 kV. High-resolution transmission electron microscopy (HRTEM) and transmission electron microscopy-energy dispersive X-ray spectroscopy (TEM-EDX), SAED, and bright-field and dark-field TEM analyses were performed in a TEM (Tecn F20) with an accelerating voltage of 200 kV. X-ray photoelectron spectroscopy (XPS) studies were performed using PHI5000 VersaProbe. The binding energy data were calibrated relative to the C 1s signal at 284.6 eV. In the XPS depth profile studies, the etched depth is ~3–5 nm in each round of the soft Ar etching. X-ray powder diffraction (XRD) was carried out with a Bruker D8 Advance X-ray diffractometer using Cu K α radiation at a scanning rate of 9°/min in the 2 θ range from 20° to 80°.

Electrochemical experiments. The CO₂R experiments were performed in the KHCO₃ and KOH electrolytes in a flow-cell device with a three-electrode setup. Different volumes of 10 M KOH were added to 1 M KHCO₃ solution to adjust the pH to 11, 12, 13, and 14, respectively, confirming with a pH meter. An Ag/AgCl (in saturated KCl) electrode was used as a reference electrode; a nickel foam was used as a counter-electrode; Sn, Bi, and Bi_xSn electrodes were used as working electrodes. The three electrodes were connected to an electrochemical workstation (Metrohm Autolab). The flow rate of CO₂ was set to 20–50 mL min⁻¹ under standard conditions at the outlet end of the flow cell for all the experiments. The gaseous products were quantified using gas chromatography (GC, PerkinElmer) with a thermal conductivity detector (TCD) and a flame ionization detector (FID). The liquid products were detected using nuclear magnetic resonance (NMR, Bruker 400 M) with water peak suppression. To determine the Faraday efficiency of the liquid products, we quantified the liquid products in both analytes and catholyte by NMR. The electrolytes (on both sides) are also replaced at regular time intervals before the NMR tests. The CO₂R performance of Bi, Sn, and Bi_{0.1}Sn catalysts was also evaluated in MEA electrolyzers. A commercial CO₂R MEA electrolyser (Dioxide Materials) was used to accommodate the electrochemical reactions. The MEA electrolyser was composed of anode and cathode flow field plates with a serpentine-configuration flow field of 5 cm² for the continuous supply of anolyte (0.1 M KHCO₃) and humidified CO₂ to each respective electrode. We used Bi/PTFE, Sn/PTFE, and Bi_{0.1}Sn/PTFE as the cathode, an iridium oxide deposited titanium foam as the anode, and a solid-state cation-exchange membrane (CEM) for HCOO⁻ placed in between the cathode and anode. Before the electrochemical testing, the cathode electrodes (Bi, Sn, or Bi_{0.1}Sn on PTFE) were taped to the stainless-steel flow field plate by using a copper frame for homogeneously distributing the electrical current. The anode (IrO_x on Ti foam) and cathode were physically separated by CEM (Nafion™ 117, Fuel Cell Store) in the solid-state CEM-based MEA experiments and by AEM (Sustainion X37-50 membrane) in the AEM-based MEA experiments. Electrolyser bolts were tightened by applying an equal compression torque. Before experiments, the AEM was activated in 1 M KOH for more than 24 h. Upon completion of the electrolyser assembly, the anolyte (0.1 M KHCO₃) flowed through the anode with a constant flow rate of 15 mL min⁻¹, while the humidified CO₂ was supplied from the gas diffusion electrode (GDL) back with a constant flow rate of 60 standard cubic centimetres per minute (sccm). The full-cell potentials are presented without IR correction. The gas samples were examined using GC (PerkinElmer Clarus 680) to calculate the FE of gas products. The liquid product, formate (when collected from the anodic stream from the AEM-based MEA) or HCOO⁻ (when collected from the cathodic stream from the solid-state CEM-based MEA), was collected from the anodic and cathodic streams simultaneously and analysed by an NMR spectroscopy (Agilent DD2 600 MHz) by using dimethylsulfoxide (DMSO) as the internal standard. The FE towards formate or formic acid at each current density was calculated by adding up both anodic and cathodic FEs. More details are discussed in the supplementary information.

Density functional theory (DFT) calculation. The facets Bi (003), Sn (200), and Sn (101) are primarily exposed in the Bi, Sn, and Bi_{0.1}Sn catalysts (Fig. 1); these facets were thus used to build the DFT models (Supplementary Fig. 10, Supplementary Table 1). We incorporated 1–8 Bi into 64 Sn crystals, as more than 8 Bi would de-stabilize the Sn crystal structure (Supplementary Figs. 12–15). All DFT calculations were performed with the Vienna ab initio simulation package (VASP)⁴³. The DFT calculation details are included in the Supplementary Information.

Data availability

Source data to generate figures and tables are available from the corresponding authors.

Received: 24 February 2021; Accepted: 28 July 2021;

Published online: 01 September 2021

References

1. Bushuyev, O. S. et al. What should we make with CO₂ and how can we make it? *Joule* **2**, 825–832 (2018).
2. De Luna, P. et al. What would it take for renewably powered electrosynthesis to displace petrochemical processes? *Science* **364**, 350 (2019).
3. Grasemann, M. & Laurenczy, G. Formic acid as a hydrogen source—recent developments and future trends. *Energy Environ. Sci.* **5**, 8171–8181 (2012).
4. Mellmann, D., Sponholz, P., Junge, H. & Beller, M. Formic acid as a hydrogen storage material - development of homogeneous catalysts for selective hydrogen release. *Chem. Soc. Rev.* **45**, 3954–3988 (2016).
5. Ross, M. B. et al. Designing materials for electrochemical carbon dioxide recycling. *Nat. Catal.* **2**, 648–658 (2019).
6. Fan, L. et al. Electrochemical CO₂ reduction to high-concentration pure formic acid solutions in an all-solid-state reactor. *Nat. Commun.* **11**, 3633 (2020).
7. Kibria, M. G. et al. Electrochemical CO₂ reduction into chemical feedstocks: from mechanistic electrocatalysis models to system design. *Adv. Mater.* **31**, 1807166 (2019).
8. Liu, X.-Q., Wu, Y.-T., Chen, W.-K. & Yu, Z.-L. Concurrent synthesis of methanol and methyl formate catalyzed by copper-based catalysts in a slurry phase. In *Natural Gas Conversion V, Proc. 5th International Natural Gas Conversion Symposium* **119**, 557–560 (1998).
9. Rong, L., Xu, Z., Sun, J. & Guo, G. New methyl formate synthesis method: coal to methyl formate. *J. Energy Chem.* **27**, 238–242 (2018).
10. Boddien, A. et al. Kohlenstoffdioxid-neutrale Wasserstoffspeicherung basierend auf Bicarbonaten und Formiaten. *Angew. Chem.* **123**, 6535–6538 (2011).
11. Jouny, M., Luc, W. & Jiao, F. General techno-economic analysis of CO₂ electrolysis systems. *Ind. Eng. Chem. Res.* **57**, 2165–2177 (2018).
12. Verma, S. et al. A gross-margin model for defining technoeconomic benchmarks in the electroreduction of CO₂. *ChemSusChem* **9**, 1972–1979 (2016).
13. Gong, Q. et al. Structural defects on converted bismuth oxide nanotubes enable highly active electrocatalysis of carbon dioxide reduction. *Nat. Commun.* **10**, 2807 (2019).
14. He, S. et al. The p-orbital delocalization of main-group metals to boost CO₂ Electroreduction. *Angew. Chem. Int. Ed. Engl.* **57**, 16114–16119 (2018).
15. Zhang, S., Kang, P. & Meyer, T. J. Nanostructured tin catalysts for selective electrochemical reduction of carbon dioxide to formate. *J. Am. Chem. Soc.* **136**, 1734–1737 (2014).
16. Wen, G. et al. Ternary Sn-Ti-O electrocatalyst boosts the stability and energy efficiency of CO₂ reduction. *Angew. Chem. Int. Ed. Engl.* **59**, 12860–12867 (2020).
17. Yoo, J. S. et al. Theoretical insight into the trends that guide the electrochemical reduction of carbon dioxide to formic acid. *ChemSusChem* **9**, 358–363 (2016).
18. Feaster, J. T. et al. Understanding selectivity for the electrochemical reduction of carbon dioxide to formic acid and carbon monoxide on metal electrodes. *ACS Catal.* **7**, 4822–4827 (2017).
19. Luc, W. et al. Ag-Sn bimetallic catalyst with a core-shell structure for CO₂ reduction. *J. Am. Chem. Soc.* **139**, 1885–1893 (2017).
20. Ye, K. et al. In situ reconstruction of a hierarchical Sn-Cu/SnO_x core/shell catalyst for high-performance CO₂ electroreduction. *Angew. Chem. Int. Ed. Engl.* **59**, 4814–4821 (2020).
21. Xing, Y. et al. Bi@Sn core-shell structure with compressive strain boosts the electroreduction of CO₂ into formic acid. *Adv. Sci.* **7**, 1902989 (2020).
22. Wen, G. et al. Orbital interactions in Bi-Sn bimetallic electrocatalysts for highly selective electrochemical CO₂ reduction toward formate production. *Adv. Energy Mater.* **8**, 1802427 (2018).

23. Tang, J. et al. Advantages of eutectic alloys for creating catalysts in the realm of nanotechnology-enabled metallurgy. *Nat. Commun.* **10**, 4645 (2019).
24. Yang, H., Kaczur, J. J., Sajjad, S. D. & Masel, R. I. Electrochemical conversion of CO₂ to formic acid utilizing Sustainion™ membranes. *J. CO₂ Util.* **20**, 208–217 (2017).
25. Lei, F. et al. Metallic tin quantum sheets confined in graphene toward high-efficiency carbon dioxide electroreduction. *Nat. Commun.* **7**, 12697 (2016).
26. Li, F. et al. Hierarchical mesoporous SnO₂ nanosheets on carbon cloth: a robust and flexible electrocatalyst for CO₂ reduction with high efficiency and selectivity. *Angew. Chem. Int. Ed. Engl.* **56**, 505–509 (2017).
27. Xia, C. et al. Continuous production of pure liquid fuel solutions via electrocatalytic CO₂ reduction using solid-electrolyte devices. *Nat. Energy* **4**, 776–785 (2019).
28. Vasileff, A. et al. Surface and interface engineering in copper-based bimetallic materials for selective CO₂ electroreduction. *Chem* **4**, 1809–1831 (2018).
29. Wang, Y. et al. Defect and interface engineering for aqueous electrocatalytic CO₂ reduction. *Joule* **2**, 2551–2582 (2018).
30. Zhong, M. et al. Surface modification of CoO_x loaded BiVO₄ photoanodes with ultrathin p-type NiO layers for improved solar water oxidation. *J. Am. Chem. Soc.* **137**, 5053–5060 (2015).
31. Zhong, M. et al. Accelerated discovery of CO₂ electrocatalysts using active machine learning. *Nature* **581**, 178–183 (2020).
32. Dinh, C. T. et al. CO₂ electroreduction to ethylene via hydroxide-mediated copper catalysis at an abrupt interface. *Science* **360**, 783–787 (2018).
33. Koh, J. H. et al. Facile CO₂ electro-reduction to formate via oxygen bidentate intermediate stabilized by high-index planes of Bi dendrite catalyst. *ACS Catal.* **7**, 5071–5077 (2017).
34. Li, F. et al. Towards a better Sn: efficient electrocatalytic reduction of CO₂ to formate by Sn/SnS₂ derived from SnS₂ nanosheets. *Nano Energy* **31**, 270–277 (2017).
35. Yang, H. et al. Selective CO₂ reduction on 2D mesoporous Bi nanosheets. *Adv. Energy Mater.* **8**, 1801536 (2018).
36. Han, N. et al. Ultrathin bismuth nanosheets from in situ topotactic transformation for selective electrocatalytic CO₂ reduction to formate. *Nat. Commun.* **9**, 1320 (2018).
37. Yang, Q. et al. Novel Bi-doped amorphous SnO_x nanoshells for efficient electrochemical CO₂ reduction into formate at low overpotentials. *Adv. Mater.* **32**, 2002822 (2020).
38. García de Arquer, F. P. et al. CO₂ electrolysis to multicarbon products at activities greater than 1 A cm⁻². *Science* **367**, 661–666 (2020).
39. Yang, K., Kas, R. & Smith, W. A. In situ infrared spectroscopy reveals persistent alkalinity near electrode surfaces during CO₂ electroreduction. *J. Am. Chem. Soc.* **141**, 15891–15900 (2019).
40. Wang, G., Pan, J., Jiang, S. P. & Yang, H. Gas phase electrochemical conversion of humidified CO₂ to CO and H₂ on proton-exchange and alkaline anion-exchange membrane fuel cell reactors. *J. CO₂ Util.* **23**, 152–158 (2018).
41. Zheng, X. et al. Sulfur-modulated tin sites enable highly selective electrochemical reduction of CO₂ to formate. *Joule* **1**, 794–805 (2017).
42. García de Arquer, F. P. et al. 2D metal oxyhalide-derived catalysts for efficient CO₂ electroreduction. *Adv. Mater.* **30**, e1802858 (2018).
43. Kresse, G. & Hafner, J. Ab initio molecular-dynamics simulation of the liquid-metal–amorphous–semiconductor transition in germanium. *Phys. Rev. B* **49**, 14251–14269 (1994).

Acknowledgements

This work was supported financially by the National Key R&D Program of China (No. 2020YFA0406102), the National Natural Science Foundation of China (grant number 91963121), the Natural Science Foundation of Jiangsu Province (Grant No. BK20190056), and the Frontiers Science Center for Critical Earth Material Cycling of Nanjing University. Parts of the calculations were performed using computational resources on an IBM Blade cluster system from the High-Performance Computing Center (HPCC) of Nanjing University. We thank Yimeng Min, Christine Gabardo, and Ziyun Wang for discussions during the study.

Author contributions

M.Z. and E.H.S. supervised the project. M.Z. conceived the idea and designed the experiments. L.L. conducted the synthesis, characterizations, and flow-cell tests. L.L., A.O., F.P.G.A., Ming-Z., J.Z., H.J., C.W. and M.Z. discussed the experiment results. A.O., F.P.G.A. and D. S. designed and carried out the MEA tests. S.G., W.W., and H.D. carried out the DFT calculations. S.G., L.L., M.Z., W. W. and H.D. discussed the DFT results. M.Z., A.O., F.P.G.A., L.L. and E.H.S. wrote the manuscript. All authors discussed the results and assisted during manuscript preparation.

Competing interests

The authors declare no competing interests.

Additional information

Supplementary information The online version contains supplementary material available at <https://doi.org/10.1038/s41467-021-25573-9>.

Correspondence and requests for materials should be addressed to H.D., E.H.S. or M.Z.

Peer review information *Nature Communications* thanks the other anonymous reviewers for their contribution to the peer review of this work.

Reprints and permission information is available at <http://www.nature.com/reprints>

Publisher's note Springer Nature remains neutral with regard to jurisdictional claims in published maps and institutional affiliations.



Open Access This article is licensed under a Creative Commons Attribution 4.0 International License, which permits use, sharing, adaptation, distribution and reproduction in any medium or format, as long as you give appropriate credit to the original author(s) and the source, provide a link to the Creative Commons license, and indicate if changes were made. The images or other third party material in this article are included in the article's Creative Commons license, unless indicated otherwise in a credit line to the material. If material is not included in the article's Creative Commons license and your intended use is not permitted by statutory regulation or exceeds the permitted use, you will need to obtain permission directly from the copyright holder. To view a copy of this license, visit <http://creativecommons.org/licenses/by/4.0/>.

© The Author(s) 2021